**Proceedings 10th NUMGE 2023**
10th European Conference on Numerical Methods in Geotechnical Engineering
Zdravković L, Konte S, Taborda DMG, Tsiampousi A (eds)
ISSN

doi: 10numge-2023-Y-XXXX

# 3D FE simulation of an instrumented monopile under quasi-static loading

A.Kheffache[1] , B. Stuyts[1,2] , C. Sastre Jurado[1,2], W. Weijtjens[2], C. Devriendt[2]
[1]*UGent Geotechnical Laboratory, OWI-lab, Technologiepark 68, Zwijnaarde, 9052, Belgium*
[2]*Vrije Universiteit Brussel, OWI-lab, Pleinlaan 2, 1050, Brussels, Belgium*

**ABSTRACT:** Monitoring accumulated data over years of operation of monopile-supported offshore wind turbines (OWTs) show a global mismatch between the as-designed and the actual performance of monopiles. This mismatch is due to the fact that design methodologies that were used are not suited for large-diameter piles. This mismatch is demonstrated, both in terms of natural frequency and bending moments in the pile. A 3D Finite Element (FE) model is developed in ABAQUS to simulate the response under quasi-static thrust loading for an instrumented monopile foundation located in the Belgium North Sea. The soil medium is modelled using the Hypoplastic constitutive model for sand and clay, and is calibrated using collected soil data from the Belgian North Sea. The developed FE model is used along with the calibrated soil models to investigate the monopile response under quasi-static load levels. The performance of the numerical model is evaluated by comparing the numerical results with the monitoring data.

**Keywords:** Monopile; Monitoring; Bending moment; Finite elements

## 1 INTRODUCTION

Nowadays, monopile supported offshore wind turbines account for 80% of the total installed structures. This has motivated a number of research initiatives such as the recently completed PISA project (Burd et al., 2020; Byrne et al., 2020), where a new design methodology was proposed for laterally loaded monopiles under monotonic conditions through field testing on monopiles with outer diameters up to 2.5m. Leblanc et al. (2010) investigated the Serviceability Limit State (SLS) performance of monopiles using scale-model testing, where the monopile rotation should be kept under a threshold value in order to avoid excessive tilt of the turbine.

Next generation wind turbines are going to have monopiles with even larger diameter (up to 10m) and are going to be placed in deeper water depths, which will make them prone to low frequency excitations such as wind and wave loadings.

The SOILTWIN project is a research project that aims to bring the cost of offshore energy down by addressing the mismatch between the as-designed and the as-build dynamics of OWTs (www.owi-lab.be/soiltwin). In the context of this project, monopiles are looked at from a Fatigue Limit State (FLS) perspective. Several wind turbines have been instrumented with accelerometers, strain gauges (SGs) and Fiber Bragg Grating fibre optic sensors (FBGs)(Stuyts et al., 2020), an example of instrumented monopile is given in Figure 1. The extracted monitoring data is then used to gain insight on the evolution of the wind turbines stiffness over their operational life. Moreover, the use of 3D Finite Element Method (FEM) is getting increasingly adopted in both industry and research as the 3D soil-wind turbine interactions are too complex to be fully and accurately captured by 1D approaches (Doherty and Gavin, 2012) .

The objective of this paper is to investigate the response of a laterally loaded monopile under quasi-static conditions in terms of bending moment using 3D finite element analysis and advanced soil constitutive models. The FE results are then compared to monitoring data gathered from wind turbines located in the Belgian north sea.

*Figure 1. Inside view of an instrumented monopile, black lines are optical fibres on which the FBGs are mounted at different depths.*

## 2 MODELING OF WIND TURBINES

Two modelling approaches are generally adopted for offshore wind turbines. The first approach consists in

discretizing the soil with non-linear spring elements (for example : lateral springs $p-y$ and rotational springs $M-\theta$). This method has been recommended in offshore codes for the design of laterally loaded piles (API, 2011) and is widely adopted in the industry due to the low computational cost associated to it. The recommendations have been proven to be unreliable for the design of monopiles, as they were originally formulated for more slender piles (Doherty and Gavin, 2012). The second approach is to model both the soil medium and the wind turbine using 3D-FEM. The soil behaviour is captured using constitutive models that needs to be calibrated using advanced laboratory test results. Although this approach is more advanced than the first one, the difficulty associated with it is greater as :

- The constitutive models choice and their calibration can have a tremendous effect on the performance of the 3D-FEM analysis
- More advanced laboratory testing data is needed to build 3D models as compared to 1D models
- The 3D model boundary conditions needs to accurately be representative of the in-situ ones
- The computational cost is higher

The PISA project design methodology can be considered as a hybrid method, as it formulates guidance for 1D response curves but allows these curves to be updated using site-specific FE models. It thus takes the advantage of both methods (low computational cost of the first method and the accuracy of the second method).

## 3 SITE CONDITIONS

### *3.1* Monopile

The instrumented pile used in this study is located in the Belgian North Sea. A total of 4 sets of FBGs are attached to the monopile below the mudline level. Micro strains recordings can then be transformed into bending moments, after the determination of dominant wind direction (Henkel et al., 2018). The above mudline level is also instrumented with Strain gauges and FBGs. The pile normalized geometry parameters are given in Table 1.

*Table 1. Monopile geometric characteristics, Where D is the monopile diameter, L is the below mudline monopile length, and t is the monopile's wall thickness.*

| $L/D$ | $D/t$ |
|---|---|
| 5.8 | 50-87.7 |

### *3.2* Scour protection

The monopile is surrounded by a rock armour-type scour protection that is composed of two layers: a filter layer and a rock armour layer.

### *3.3* Soil conditions

The instrumented monopile is embedded in a multilayer soil made of sand and clay layers. The geotechnical soil profile was established by using the in-situ campaign test data and from the interpretation of the available boreholes near the monopile location. A total of 6 soil layers have been identified as shown in Figure 2.

### *3.4* Monopile loading

The OWTs are equipped with a Supervisory Control And Data Acquisition (SCADA) system. This system is continuously gathering data over time such as the wind and rotor speeds. Loadings on the monopile were derived using the SCADA and Metocean data. A total of 11 monitored load cases ($LC$) were considered in this work ($LC0$ to $LC10$). Every load case was assumed to be quasi-static: time intervals $\Delta t$ where wind speed $U$ was observed to have little variation were selected (see Sastre Jurado et al. (2022) for more details on the load derivation methodology). The monitored loads consist of a lateral force and a point moment couple $(F, M)$ applied at the monopile's head as shown on Figure 2. The loading intensity for $LC10$ is the highest, whereas the intensity for $LC0$ is the lowest ($F_{LC10} > F_{LC0}$ and $M_{LC10} > M_{LC0}$). The strain measurements along the OWTs for the same time intervals $\Delta t$ are converted into bending moments. Every monitored load case is paired with a monitored bending moment profile. The load cases are going to be applied on a monopile model to produce numerical bending moments which are then be compared to the monitored ones.

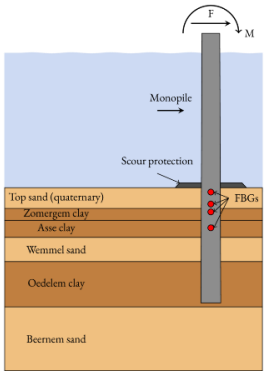


*Figure 2. Layout of instrumented monopile, soil stratigraphy and loading on the monopile.*

## 4 3D-FE MODEL / CONSTITUTIVE MODELING

The ABAQUS software is used to model the given problem. The soil and monopile have been modelled as different parts and the interaction between the different parts is considered. The scour protection was not modelled. Only half of the problem is modelled as only the lateral loads were considered (along the x axis in Figure 3).

### *4.1* Monopile

The monopile is modelled using C3D8 mesh elements, which are 3D continuum 8 nodes fully integrated linear brick elements. The modelled monopile is idealised as having a constant wall thickness (constant monopile inertia $I_P$). An elastic behaviour is assigned to the monopile with a constant Poisson's ratio of 0.3 and a Young's modulus $E_P$ that varies with depth (between 150 and 260 $GPa$) in order to produce a comparable bending stiffness $E_P I_P$ between the monitored and the simulated monopile.

### *4.2* Soil

Soil elements are modelled using C3D8 mesh elements. The soil clay and sand layers are modelled using the clay and sand hypoplasticity models respectively (Mašín, 2013; Wolffersdorff, 1996). The constitutive models have been previously calibrated for all the 6 layers shown in Figure 2. The constitutive models are available in form of user defined material (UMAT) Fortran files at soilmodels.com (Gudehus et al., 2008). Both UMATs for clay and sand were combined into one UMAT file. The soil stress is initialized in the model considering a $K_0$ initial state, where $K_0$ is the earth pressure coefficient at rest, and is given by:

$$K_{0,sand} = 1 - \sin(\varphi_c) \quad (1)$$

$$K_{0,clay} = (1 - \sin(\varphi_c)\, OCR^{\sin(\varphi_c)} \quad (2)$$

where $\varphi_c$ is the critical friction angle and $OCR$ is the overconsolidation ratio interpreted from oedometer tests. The initial void ratio is interpreted from a water content profile at a nearby borehole. A drained behaviour is assigned to the sand layers and an undrained behaviour is assigned to the clay layers.

Both the monopile and soil mesh are shown in Figure 3.

### *4.3* Interface

The general contact algorithm is used. This algorithm assumes that every part that forms the global model (monopile part and soil part) are in contact, without the need to manually define the contact pairs. The Contact interaction between the soil and the monopile was modelled using a Mohr-Coulomb frictional coefficient $\mu$. The general contact algorithm only allows to use one frictional coefficient in the whole model. A sensitivity analysis was performed on its value and it was found that it has no effect on the results (Kim and Jeong, 2011). A value of $\mu = 0.5$ is selected over the embedded monopile length.

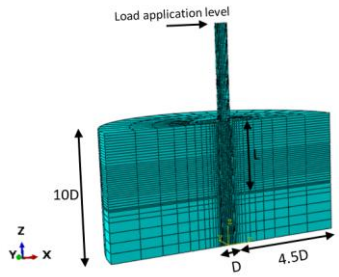


*Figure 3. 3D FE mesh*

### *4.4* Constitutive models and their calibration

#### *4.4.1* Brief description

The main features of most elastoplastic models are: the yield surface, the plastic potential, the decomposition of strain to elastic and plastic parts, the hardening and flow rule. The hypoplastic models are different from the elastoplastic ones as no distinction is made between the elastic and plastic strain. The concept of yield and plastic potential surfaces isn't required in the hypoplasticity framework.

The general hypoplasticity formulation as proposed by Gudehus (1996) is given by the following equation:

$$\dot{T} = f_s(\mathcal{L} : D + f_d N \|D\|) \quad (3)$$

where the scalar factor $f_s$ is the barotropy factor that takes into account the effect of mean pressure, $\mathcal{L}$ is a fourth-order tensor, $D$ is the stretching tensor, the scalar factor $f_d$ is the pyknotropy factor that takes into account the effect of void ratio and $N$ is a second-order tensor. The previous scalars and tensors are expressed using the basic hypoplasticity parameters for the sand and clay models (see Mašín (2019) for more details). The basic hypoplastic models have been enhanced with the concept of Intergranular Strain to better capture the small strain stiffness of soils (Niemunis and Herle, 1997). This enhancement adds new sets of parameters to the constitutive models to be calibrated.

#### *4.4.2* Calibration

For the sake of brevity, only the calibration of the top sand (quaternary) and the zomergem clay layers will be shown. The calibrated parameters are given in Table 2 to Table 6.

The hypoplastic sand model is composed of 8 basic parameters ($\varphi_c$, $h_s$, $n$, $e_{c0}$, $e_{d0}$, $e_{i0}$, $\beta$, and $\alpha$) and 5 Intergranular Strain parameters ($m_R$, $m_T$, $R$, $\beta_R$ and $\chi$). The basic parameters are calibrated according to the methodology proposed by Herle and Gudehus (1999). The critical state friction angle is determined using reconstituted- consolidated triaxial tests, only the tests where the axial strain reached large enough values were selected. The critical stress ratio in compression is given by $M_c = q/p'$ and the critical friction angle is given by

$\varphi_{cs} = \arcsin(\frac{3M_c}{6+M_c})$ (Figure 4a). The critical state line (CSL) can be identified using drained and undrained triaxial test results on initially loose specimens (relative density $D_r$ <30%). The $e_{c0}$ parameter specifies the position of the CSL in the $p$ vs $e$ plane, Li and Wang (1998) proposed the following non-linear formula to represent it :

$$e_c = e_{c0} - \lambda\left(\frac{p'}{p'_{ref}}\right)^{\xi} \quad (4)$$

where $e_{c0}$, $\lambda$ and $\xi$ are obtained using least-squares method. It can be seen from Figure 4b that the critical state line is not perfectly defined, as most of the drained triaxial tests were performed on initially medium to high relative density ($54\% < D_r < 91\%$) in order to be representative of the in-situ relative densities. The minimum and maximum void ratios can be approximated using the recommendations of Herle and Gudehus (1999), who proposed the following analytical relationships:

$$e_{i0} = 1.2e_{c0} \quad (5)$$

$$e_{d0} = 0.5e_{c0} \quad (6)$$

Where $e_{i0}$ and $e_{d0}$ are the maximum and minimum void ratios zero pressure. An alternative method is to assume that $e_{c0} = e_{max}$ and $e_{d0} = e_{min}$, this method was used when the determination of $e_{c0}$ was not possible using triaxial tests. The $h_s$ and $n$ parameters control the shape of the limiting void ratio curves ($e_{i0}$, $e_{c0}$ and $e_{d0}$), they are calibrated using oedometer test results (Figure 4c). The $\alpha$ and $\beta$ parameters control the peak friction angle and the bulk/shear stiffness respectively, and are calibrated using drained triaxial test results (Figure 4d and e). The $m_R$ parameter controls the dependency of the initial shear stiffness $G_{max}$ on the mean effective pressure $p'$. It is calibrated to bender element (BE)/resonant column (RC) test results (Figure 4f). The calibrated value was further optimized to match the $G_{max}$ profile interpreted from seismic and piezocone penetration tests (CPTu and SCPT). The *R* parameter controls the size of the elastic range within the hypoplastic framework, a value of $10^{-4}$ is selected following the recommendations (Mašín, 2019). $\chi$ and $\beta_r$ control the rate of stiffness degradation with strain, they are calibrated in a trial and error fashion (Figure 4g).

The hypoplastic clay model is composed of 5 basic parameters ($\varphi_c$,$\nu$ , $N$, $\lambda^*$ and $\kappa^*$), 6 intergranular strain parameters ($A_g$, $n$, $m_{rat}$, $R$, $\beta_R$ and $\chi$) and 3 small strain stiffness anisotropy parameters ($\alpha_e$, $\alpha_g$ and $\alpha_v$). The critical state friction angle is calibrated using direct simple shear (DSS) test results at large strain (Figure 5a). Two possibilities are given for the determination of $\varphi_c$: 1) the horizontal plane is a plane of failure (maximum obliquity) which implies that $\varphi_c = \arctan(\tau_f/\sigma_{vf})$; where $\tau_f$ is the horizontal shear stress at large strain and $\sigma_{vf}$ is the corresponding vertical stress. 2) the horizontal plane is a plane of maximum shear stress, which implies that $\varphi_c = \arcsin(\tau_f/\sigma_{vf})$. The former case was assumed as it gives a conservative value. The $\nu$ parameter controls the shear stiffness, it can also be calibrated using DSS test results, a value of 0.1 was selected (Figure 5b and c). $N$ controls the intersection of the isotropic normal line and $\lambda^*$ controls its slope while $\kappa^*$controls the slope of the unloading isotropic line. They are calibrated using oedometer test results (Figure 5d). $A_g$ and $n$ control the dependency of $G_{max}$ on $p'$ (similarly to $m_R$ for sand hypoplasticity) using the following formula:

$$G_{max} = A_g p_r \left(\frac{p}{p_r}\right)^{n_g} \quad (7)$$

Where $p_r$ is a reference pressure set equal to $1\,kPa$. They are calibrated using bender element/resonant column tests (Figure 5e) by curve fitting the previous formula to the results. $R$, $\chi$ and $\beta_r$ parameters have the same meaning as for sand hypoplasticity and are calibrated the same way (Figure 5f). The $\alpha_e$ parameter controls the anisotropy in shear stiffness and is defined as : $\alpha_g = G_{pp0}/G_{tp0}$, where $G_{pp0}$ is the shear stiffness in the plane of isotropy and $G_{tp0}$ is the shear stiffness in the transverse direction. It is calibrated using bender element test where the shear wave velocity is measured in two perpendicular directions, for different means effective pressures (Figure 5g), the other anisotropy parameters are set to default values.

*Table 2. Basic hypoplastic parameters for the top sand*

| $\varphi_c°$ | $h_s(kPa)$ | $n$ | $e_{i0}$ | $e_{c0}$ | $e_{d0}$ | $\alpha$ | $\beta$ |
|---|---|---|---|---|---|---|---|
| 31.89 | 3.8e6 | 0.44 | 1.02 | 0.85 | 0.42 | 0.17 | 1 |

*Table 3. Intergranular parameters for the top sand*

| $m_R$ | $m_T$ | $R$ | $\beta_r$ | $\chi$ |
|---|---|---|---|---|
| 5 | 2 | 0.0001 | 0.1 | 1 |

*Table 4. Basic hypoplastic parameters for the zomergem clay*

| $\varphi_c°$ | $\lambda$ | $\kappa$ | $N$ | $\nu$ |
|---|---|---|---|---|
| 34.28 | 0.08 | 0.02 | 1.033 | 0.1 |

*Table 5. Intergranular parameters for the zomergem clay*

| $A_g$ | $n$ | $m_{rat}$ | $R$ | $\beta_r$ | $\chi$ |
|---|---|---|---|---|---|
| 1675 | 0.72 | 0.7 | 0.0001 | 0.3 | 3 |

*Table 6. Anisotropic stiffness parameters for the zomergem clay*

| $\alpha_e$ | $\alpha_v$ | $\alpha_g$ |
|---|---|---|
| 1 | 1 | 1.56 |

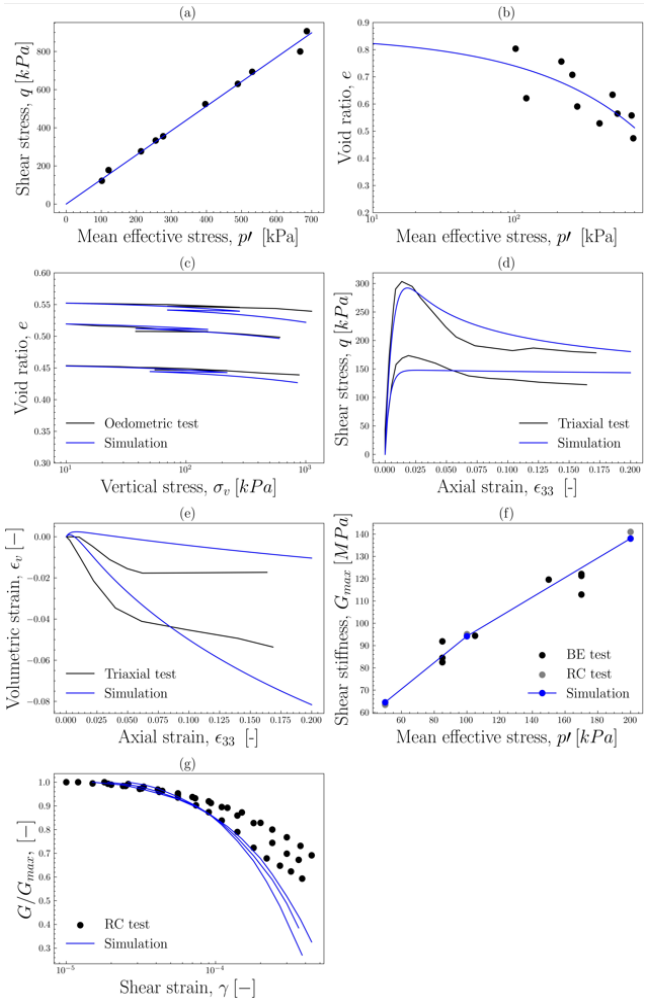


*Figure 4. Calibration of sand hypoplasticity parameters for the top quaternary later*

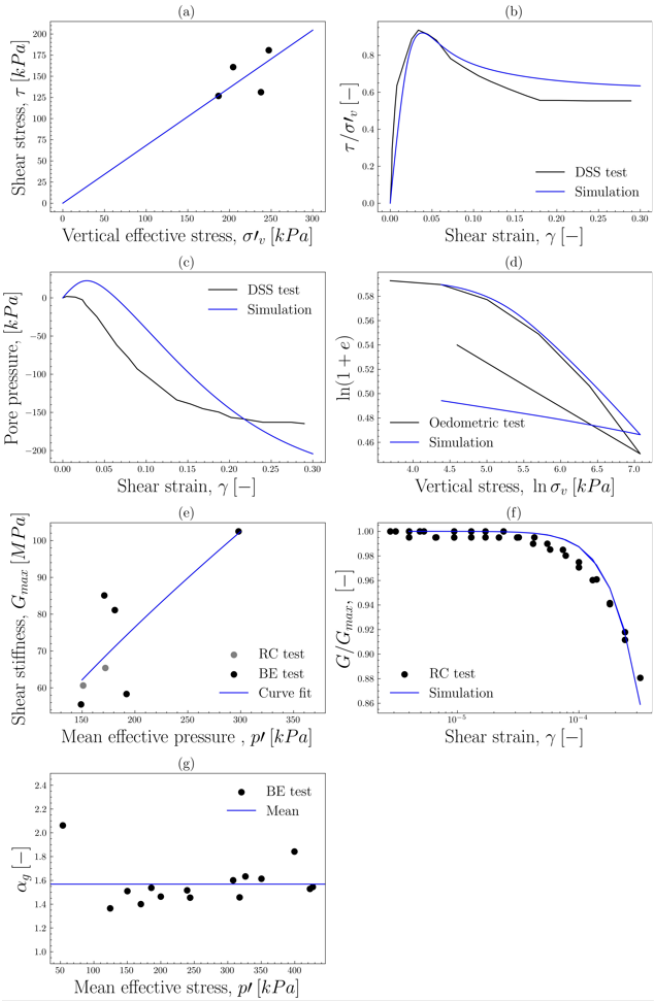


*Figure 5. Calibration of clay hypoplasticity parameters for the zomergem layer*

## 5 NUMERICAL MODELING RESULTS AND COMPARISON WITH MONITORED BENDING MOMENTS

The comparison between modelling results and the monitored bending moment is done at every sensor depth on the monopile below the mudline level. 11 load cases are derived (as outlined in section 3.4) and applied on the monopile model at the load application level (Figure 3), the resulting bending moments are then extracted. The Mean Relative Error ($MRE$) is calculated at each sensor depth using the following equation:

$$MRE\_M^z = \frac{1}{11}\sum_{i=0}^{10} \frac{|M_m^{z,i} - M_s^{z,i}|}{M_m^{z,i}} \quad (8)$$

where $M_m^{z,i}$ is the monitored bending moment at the z-th sensor location of the i-th load case, $M_s^{z,i}$ is the simulation bending moment for the same load case and sensor location. The relative error is calculated for each load case, then the mean is calculated by dividing the sum of relative errors by the number of load cases.

The monitored and simulated bending moments are given in Figure 6, only the response of 3 out of the 11 load cases (LC0, LC4 and LC10) are shown for clarity. The monitored and simulated bending moments are normalized with regards to the highest monitored bending moment value (corresponding to LC10 at the first sensor depth, which is why the normalized monitoring bending moment is equal to 1 at the 1st sensor location for LC10 in Figure 6). We can see that the simulated and monitored bending moments increase with increasing load levels. Moreover, we can also see that for the 3 plotted loads, the simulated bending moment is higher than the monitored one with an increasing mismatch with depth, and it is the case for all the monitored load cases (LC0 to LC10), which indicates an under estimation of the monopile's lateral stiffness. The $MRE$ is calculated for all load cases using Equation 8 and is plotted for all the below mudline sensors in Figure 7. The values are of 7.94, 9.53, 16.47 and 41.88% for sensor 1, 2,3 and 4 respectively, where sensor 1 is the shallowest and sensor 4 is the deepest (Figure 2). The non-zero MRE values translate the mismatch between the simulated and monitored bending moments for all the load cases, while the increasing $MRE$ value with sensor depth may translate a

less stiff deep soil layers in the numerical models compared to reality (monitoring).

## 6 CONCLUSION

In this paper, a monitored monopile located in a Belgian offshore wind farm has been studied using 3D-FE analysis combined with advanced constitutive modelling of soil and monitoring data. The constitutive models were calibrated using advanced laboratory as well as in situ tests. A total of 11 monitored load cases were derrived from the exploitation of the available data at the monopile's location. The loads were then applied on the monopile model to produce numerical bending moments, which were compared to the monitored ones. The bending moment is consistently overestimated in the numerical model, which indicates an underestimation of the monopile's lateral stiffness. This underestimation might be due to the missing contribution of the scour protection, and/or to the soil constitutive model calibration. Both possible reasons are currently being studied and will be presented in future works.

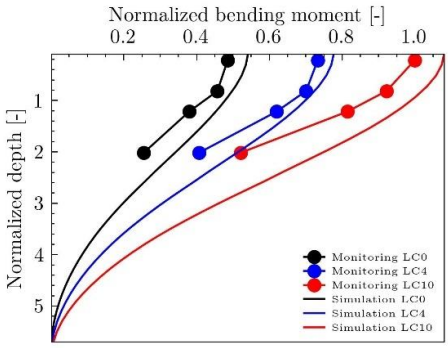


*Figure 6. Comparison between the monitored and the simulated bending moments.*

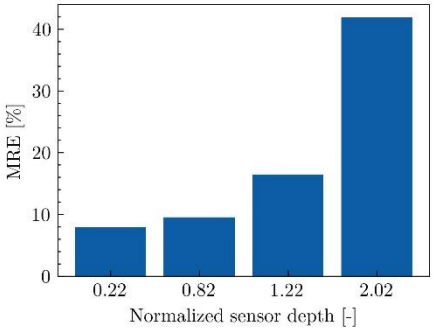


*Figure 7. MRE computed at the 4 sensors location for the 11 load cases.*

## ACKNOWLEDGEMENTS

The authors would like to acknowledge the support of the Belgian Ministry of Economic Affairs through the EFT project WINDSOIL project. The support of VLAIO through the De Blauwe Cluster SBO SOILTWIN project is also acknowledged.

## 7 REFERENCES

API. (2011). *API RP2 GEO Geotechnical and Foundation Design Considerations*.

Burd, H. J., Taborda, D. M. G., Zdravković, L., Abadie, C. N., Byrne, B. W., Houlsby, G. T., … Potts, D. M. (2020). PISA design model for monopiles for offshore wind turbines: Application to a marine sand. *Géotechnique*, *70*, 1048–1066.

Byrne, B. W., Houlsby, G. T., Burd, H. J., Gavin, K. G., Igoe, D. J. P., Jardine, R. J., … Zdravković, L. (2020). PISA design model for monopiles for offshore wind turbines: Application to a stiff glacial clay till. *Géotechnique*, *70*, 1030–1047.

Doherty, P., & Gavin, K. (2012). Laterally loaded monopile design for offshore wind farms. *Proceedings of the Institution of Civil Engineers - Energy*, *165*, 7–17.

Gudehus, G. (1996). A Comprehensive Constitutive Equation for Granular Materials. *Soils and Foundations*, *36*, 1–12.

Gudehus, Gerd, Amorosi, A., Gens, A., Herle, I., Kolymbas, D., Mašín, D., … Viggiani, G. (2008). The soilmodels.info project: LETTER TO THE EDITOR. *International Journal for Numerical and Analytical Methods in Geomechanics*, *32*, 1571–1572.

Henkel, M., Noppe, N., Weijtjens, W., & Devriendt, C. (2018). Sub-soil strain measurements on an operational wind turbine for design validation and fatigue assessment. *Journal of Physics: Conference Series*, *1037*, 052032.

Herle, I., & Gudehus, G. (1999). Determination of parameters of a hypoplastic constitutive model from properties of grain assemblies. *Mechanics of Cohesive-Frictional Materials*, *4*, 461–486.

Kim, Y., & Jeong, S. (2011). Analysis of soil resistance on laterally loaded piles based on 3D soil–pile interaction. *Computers and Geotechnics*, *38*, 248–257.

Leblanc, C., Houlsby, G. T., & Byrne, B. W. (2010). Response of stiff piles in sand to long-term cyclic lateral loading. *Géotechnique*, *60*, 79–90.

Li, X. S., & Wang, Y. (1998). Linear Representation of Steady-State Line for Sand. *Journal of Geotechnical and Geoenvironmental Engineering*, *124*, 1215–1217.

Mašín, D. (2013). Clay hypoplasticity with explicitly defined asymptotic states. *Acta Geotechnica*, *8*, 481–496.

Mašín, D. (2019). *Modelling of Soil Behaviour with Hypoplasticity: Another Approach to Soil Constitutive Modelling*. Cham: Springer International Publishing.

Niemunis, A., & Herle, I. (1997). Hypoplastic model for cohesionless soils with elastic strain range. *Mechanics of Cohesive-Frictional Materials*, *2*, 279–299.

Sastre Jurado, C., Stuyts, B., Weijtjens, W., & Devriendt, C. (2022). Impact of calibrated soil-monopile-interaction model on resonance frequencies. *Journal of Physics: Conference Series*, *2265*, 032098.

Stuyts, B., Weijtjens, W., Devriendt, C., Versteele, H., & Vanden Haute, C. (2020). Monopile lateral response calibration from in-situ monitoring data. *Proceedings of the Fourth International Symposium Frontiers in Offshore Geotechnics*. Presented at the ISFOG2020, Austin, Texas. Austin, Texas.

von Wolffersdorff, P.-A. (1996). A hypoplastic relation for granular materials with a predefined limit state surface. *Mechanics of Cohesive-Frictional Materials*, *1*, 251–271.